LETTER

All-(111) Surface Silicon Nanowires: Selective Functionalization for Biosensing Applications

M. N. Masood, S. Chen, E. T. Carlen,* and A. van den Berg

BIOS Lab on a Chip Group, MESA+ Institute for Nanotechnology, University of Twente, Enschede 7500 AE, The Netherlands

ABSTRACT We demonstrate the utilization of selective functionalization of carbon−silicon (C−Si) alkyl and alkenyl monolayers covalently linked to all-(111) surface silicon nanowire (Si-NW) biosensors. Terminal amine groups on the functional monolayer surfaces were used for conjugation of biotin n-hydroxysuccinimide ester. The selective functionalization is demonstrated by contact angle, X-ray photoelectron spectroscopy (XPS), and high-resolution scanning electron microscopy (HRSEM) of 5 nm diameter thiolated Au nanoparticles linked with streptavidin and conjugated to the biotinylated all-(111) surface Si-NWs. Electrical measurements of monolayer passivated Si-NWs show improved device behavior and performance. Furthermore, an analytical model is presented to demonstrate the improvement in detection sensitivity of the alkyl and alkenyl passivated all-(111) Si-NW biosensors compared to conventional nanowire biosensor geometries and silicon dioxide passivation layers as well as interface design and electrical biasing guidelines for depletion-mode sensors.

KEYWORDS: silicon • nanowires • Si−C monolayers • biosensing

Silicon nanowire field-effect biosensors have been reported extensively for the highly sensitive, label-free, and real time detection of biomolecular binding of ssDNA, proteins, and viruses (1−4). The high detection sensitivity of Si-NW biosensors has been attributed to the large surface-to-volume ratio and the three-dimensional multigate structure; both contribute to the improved sensitivity compared to conventional planar devices (5, 6). In this letter, we present a new Si-NW biosensor platform consisting of our recently reported all-(111) surface Si-NWs (7) with a heterogeneous alkyl and alkenyl monolayer interfaces that are suitable for functionalization with any biomolecular moiety (8), and therefore provides improved selectivity and sensitivity compared to conventional Si-NW biosensors.

Figure 1a shows an example of the Si-NW biosensor measurement configuration. The front-gate voltage V_{fg} with reference electrode and back-gate voltage V_{bg} control the operating point of the sensor.

The Si-NW channel conductance is defined as $G_c = \partial i_{ds}/\partial v_{ds}|_{V_{fg},V_{bg}}$, where i_{ds} and v_{ds} are the NW drain-to-source current and applied voltage, respectively. Biosensing is achieved when molecular binding at the sensing surface induces a surface potential change $\Delta\psi_o$ that results in a measurable conductance change ΔG_c via a field-effect across the dielectric layer (Figure 1a).

The transformation of a nanowire into a biosensor requires surface functionalization, such that biologically active ligands (9) are conjugated to the sensor surface (10, 11). Conventional Si-NW biosensors have the ligand attached directly to the SiO_2 sensor surface using silane-based attachment chemistry. However, conjugating to the SiO_2 layer reduces the sensor selectivity because the entire substrate surface is most often a homogeneous oxide surface. Selective functionalization to oxide passivated Si-NWs has been reported (12). Figure 1b shows a cross-section (A-B, Figure 1a) of a triangular Si-NW with conventional nonselective functionalization as the ligands cover the entire homogeneous surface, which drastically reduces the number of analytes (9) that bind to the sensing surface. Figure 1c shows a selectively functionalized Si-NW biosensor where the ligands are conjugated exclusively to the silicon surface and the entire surface is heterogeneously functionalized. Throughout this letter, triangular cross-sections are analyzed because they represent Si-NW biosensors developed in our laboratory; however, the analysis can be generalized to any cross-sectional shape.

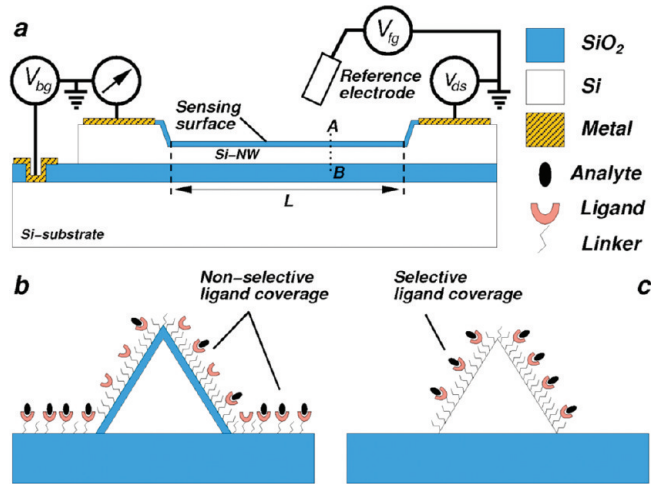

FIGURE 1. Si-NW biosensor configurations. (a) Biosensor with control voltages and current measurement. (b) Conventional nonselective homogeneous surface. (c) Selective heterogeneous functionalization with ligands conjugated exclusively to the Si-NW sensor.

* Corresponding author. E-mail: e.t.carlen@utwente.nl.
Received for review September 25, 2010 and accepted November 16, 2010
DOI: 10.1021/am100922e
2010 American Chemical Society

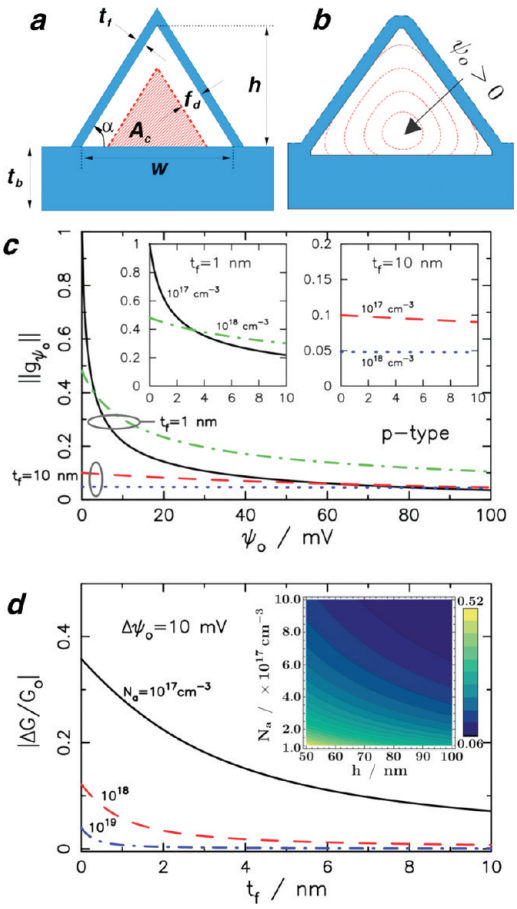

FIGURE 2. Depletion-mode p-type Si-NW transconductance and sensitivity. (a) Ideal cross-section with conduction area A_c (red hashed) (b) 2D finite element simulation result of depletion region contours (red dashed lines the edge of depletion region) as $\psi_o > 0$ (c) Normalized transconductance for $t_f = 1$ nm: $N_a = 1 \times 10^{17}$ cm^{-3} (black, solid) and 1×10^{18} cm^{-3} (green, dot-dash); $t_f = 10$ nm: $N_a = 1 \times 10^{17}$ cm^{-3} (red, dashed) and 1×10^{18} cm^{-3} (blue, dotted) (d) $|\Delta G/G_o|$ as a function of dielectric thickness for different N_a with $h = 100$ nm and $\Delta\psi_o = 10$ mV (Inset: contour map of $|\Delta G/G_o|$ for $t_f = 1$ nm showing the N_a and h dependence).

Detection sensitivity of ligand-analyte binding is dependent on the distance from the charged analyte to the silicon surface, which includes analyte, ligand, and linker (on an oxide in the conventional case) (13). We have developed an analytical model of a depletion-mode Si-NW with triangular cross-section that is used to quantitatively estimate the detection sensitivity. The body of the depletion-mode Si-NW device (Figure 1a) doped with impurities results in a quiescent channel conductance $G_c = \mu_b L^{-1} Q_c$, where μ_b is the carrier mobility, L the length, and Q_c the charge per unit length ($Q_c > 0$ for p-type and $Q_c < 0$ for n-type) (14). As previously described, a surface potential change $\Delta\psi_o$ on the sensing surface induced by an electrical charge density change $\Delta\sigma_o$ near the sensing surface during molecular binding results in the field-effect modulation of the conduction cross-sectional area A_c (red hashed region, Figure 2a), and the channel conductance is modulated $G_c \pm \Delta G_c$ where $Q_c = qN_aA_c$, N_a is the doping concentration, which is assumed to be uniformly distributed.

The conduction cross-sectional area as a function of ψ_o can be modeled as $A_c(f_d) = 1/2(w - 2f_d/\sin\alpha)(h - f_d/\cos\alpha)$ (6), where width w, height h, and base angle α are shown in Figure 2a, and $f_d = ((\varepsilon_{si}/\varepsilon_{ox}t_f)^2 + 2\varepsilon_{si}\varepsilon_o(V_{fg} - V_{fb})/qN_a)^{1/2} - \varepsilon_{si}/\varepsilon_{ox}t_f$ is the depletion function using the depletion approximation (15). The front-gate V_{fg} (Figure 1a) is used to set the operating point of the sensor and V_{fb} is the flat band voltage necessary to achieve flat energy bands at the silicon surface. Note that the back-gate control voltage V_{bg} does not appear in the conduction expression because we have assumed that the lower surface of the NW is not depleted and not electrostatically coupled to the front-gate. The flat band voltage is $V_{fb} = E_{ref} - \phi_{Si}/q - \psi_o - Q_i/C_i - \chi^{sol} - \Delta\chi$, where E_{ref} is the potential drop due to the reference electrode, ϕ_{Si} is the silicon workfunction, Q_i and C_i represent the insulator effective charge per unit area and capacitance, χ^{sol} is the surface dipole potential, and $\Delta\chi$ represents various potential drops at the interface (6). For this analysis, we assume that V_{fg} completely compensates for the various potential drops and $V_{fg} - V_{fb} \approx \psi_o$ and the effects of interface states have been neglected. Figure 2b depicts hole depletion contours from a two-dimensional finite element simulation as the oxide surface potential is varied $\psi_o > 0$. Despite rounding of the potential contours near the sharp corners, the area modulation function $A_c(f_d)$ reasonably well approximates the triangular depletion shape.

The surface potential transconductance can be estimated as $g_{\psi_o} = \partial G_c/\partial\psi_o|_{V_{ds},V_{fg},V_{bg}}$, which is used to determine the operating point ψ_{o_b} (set with V_{fg}) where g_{ψ_o} is maximum. The commonly used relative detection sensitivity can then be calculated $\Delta G/G_o = |G(\psi_{o_s}) - G_o|/G_o$, where $G_o = G(\psi_{o_b})$, and ψ_{o_s} is the surface potential following the sensing event. This behavior has been previously described for depletion-mode silicon nanowires (7). Figure 2c shows the normalized transconductance $\|g_{\psi_o}\|$ (16) as a function ψ_o for dielectric layer thicknesses $t_f = 1$ and 10 nm with $N_a = 1 \times 10^{17}$ cm^{-3} and 1×10^{18} cm^{-3}. The tranconductance with a 1 nm layer is ~10× larger than the 10 nm thick layer for the same dopant concentration, however, only for small ψ_o and all transconductances become comparable for $\psi_o > 100$ mV. The surface charge transconductance $g_{\sigma_o} = \partial G_c/\partial\sigma_o|_{V_{ds},V_{fg},V_{bg}}$ can also be estimated with use of the Grahame equation (17) $\sigma_o = (8\varepsilon_w\varepsilon_o kTc_o)^{1/2}\sinh[q\psi_o/2kT]$, for small values of ψ_o, which relates the surface charge density to the surface potential in a monovalent electrolyte, where ε_w is the permittivity of water and c_o is the ionic concentration of the electrolyte. The surface charge detection transconductance has similar behavior (Supporting Information, Figure S1). The $\Delta G/G_o$ can then be estimated, where $G_o = G(\psi_{o_b} = 0)$. Figure 2d shows the characteristics of $\Delta G/G_o$ as a function of t_f and N_a for $\Delta\psi_o = 10$ mV, typical for small analyte concentrations (18). The inset in Figure 2d shows the strong dependence of $\Delta G/G_o$ on h and N_a for fixed $t_f = 1$ nm. The sensitivity behavior is similar to previously reported measurements (13). Panels c and d in Figure 2 clearly show that thin dielectric layers result in higher detection sensitivities and three important conclusions can be drawn from this analysis. First, thin ($t_f \approx 1$ nm) dielectric layers in combination with low channel doping ($N_a = 1 \times 10^{17}$ cm^{-3}) results

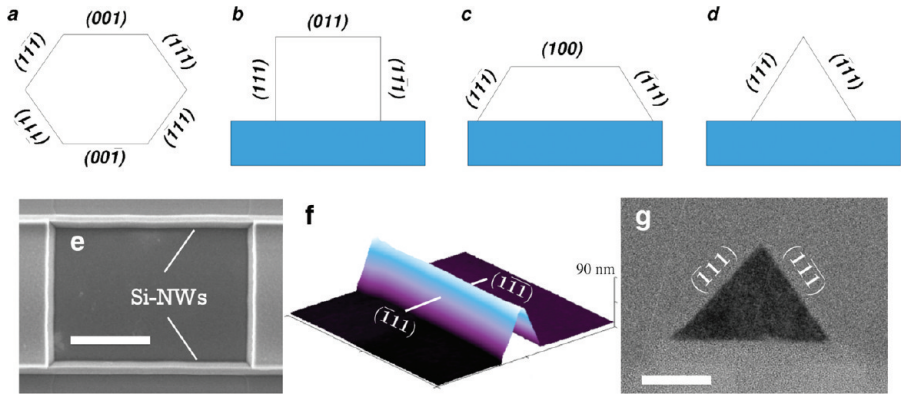

FIGURE 3. (a−d) Ideal Si-NW fabrication dependent cross-section shapes: (a) bottom-up VLS synthesized, (b) top-down rectangular, (c) top-down trapezoidal, and (d) top-down triangular. (e−g) Fabricated all-(111) surface Si-NWs: (e) high-resolution scanning electron microscopy (HRSEM) image of triangular Si-NWs (scale bar: 1 μm); (f) tapping-mode atomic force microscopy image of single Si-NW (NW height: 90 nm). (g) High-resolution transmission electron microscopy image of Si-NW cross-section (scale bar: 20 nm).

in the largest detection sensitivity, however, over a small range of ψ_o (or σ_o), and therefore, requires precise front-gate biasing for full utilization. Second, thin dielectric layers and larger channel doping ($N_a = 1 \times 10^{18}$ cm^{-3}) results in slightly lower and more uniform sensitivities. Lastly, a reference electrode is important for providing a well-defined gate potential for device biasing and operation. It should be noted that higher sensitivities can be obtained by moderately accumulating the front surfaces (6).

It is well-known that the Si (111) surface is preferred for the covalent alkylation of organic monolayers due to the surface atomic arrangement, which leads to densely packed layers and low density of dangling bonds (19−22). However, existing reports of alkyl monolayer formation on Si-NWs have been conducted on a mixture of surface orientations due to limitations in fabrication technology (2). Figure 3a−d shows cross-sections of commonly reported Si-NW shapes and the corresponding surface crystal orientation of the exposed facets, which is dependent on the fabrication technology. Bottom-up vapor−liquid−solid (VLS) synthesis of Si-NWs has been reported to have hexagonal cross-sections consisting of a mixture of surface orientations (Figure 3a) (23).

Top-down fabricated Si-NWs patterned with electron-beam lithography and formed with plane-dependent etching using Si (011) substrates (Figure 3b) (24) and Si (100) substrates (Figure 3c) (25) also have more than one type of exposed surface orientation. Alkyl monolayers have also been formed on polycrystalline silicon Si-NWs (13). Figure 3d shows the triangular Si-NW used in this letter consisting exclusively of Si (111) exposed surfaces. It should be noted that H−Si (111) surfaces have the lowest reported surface recombination velocity (26) and improved electronic performance compared to Si (100) surfaces with SiO_2 interfaces (27), and therefore, further improve the Si-NW biosensor performance. Figure 3e−g shows microscopy images of representative all-(111) surface Si-NWs fabricated with the soft top-down technology that results in Si (111) surfaces on the faces of the triangle that are atomically smooth (7). The base of the Si-NW is anchored to the SiO_2 layer of the silicon-on-insulator (SOI) substrate.

Direct covalent bonding of organic molecules to reconstructed silicon surfaces can be done using ultra high vacuum (UHV) or wet methods (8, 28). Carbon−silicon coupling reactions performed using wet chemistry methods are very attractive because of the simple apparatus required and the high reaction rates due to the presence of high reactant fluxes in solution; however, careful control of surface oxidation and cleanliness is required. The first step in forming a covalent C−Si bond is the formation of stable H−Si surfaces, which is most often done by removing the native oxide on the silicon surface with hydrofluoric acid (HF) and followed by ammonium fluoride (NH_4F) etching the silicon surface. Once a stable H−Si surface has been formed, the C−Si monolayer can be formed with an appropriate precursor and a free radical initiation using ultraviolet (UV) irradiation, heating, electrochemical reaction, transition metal complexes, or Lewis acid catalysts (29). There are many reports of C−Si monolayer formation on H−Si surfaces using different methods, such as a refluxed precursor solution of 1-hexadecene in mesitylene (30), neat solution and UV-irradiation (31), and a two-step hydrosilylation reaction with Grignard reagents (29). Monolayers formed with Grignard reagents may impart unwanted metal contaminants to the surface. Monolayers formed by Lewis acid catalysis involve lower surface coverage as compared to the coverage obtained by heating, photochemical irradiation and Grignard reaction schemes (30).

Two types of C−Si monolayers on H−Si (111) surfaces formed using photochemical UV hydrosilylation are presented in this letter. The monolayer formation with UV-initiated photochemical hydrosilylation is based on the high reactivity of the C═C bond to the bare silicon promoted by the cleavage of the H−Si at room temperature (8).

First, a C_{18} alkyl monolayer with methyl end groups was formed from a 1-octadecene precursor. The second monolayer consists of amine-terminated (NH_2) alkenyl monolayer from an n-(5-hexynyl)phthalimide precursor. Scheme 1 shows the steps used to form both monolayers. The H−Si surface is first formed followed by the UV initiated hydrosilylation with 1-octadecene and n-(5-hexynyl)phthalimide precursors to form the different monolayers. Following

Scheme 1. C—Si (111) Monolayer Formation

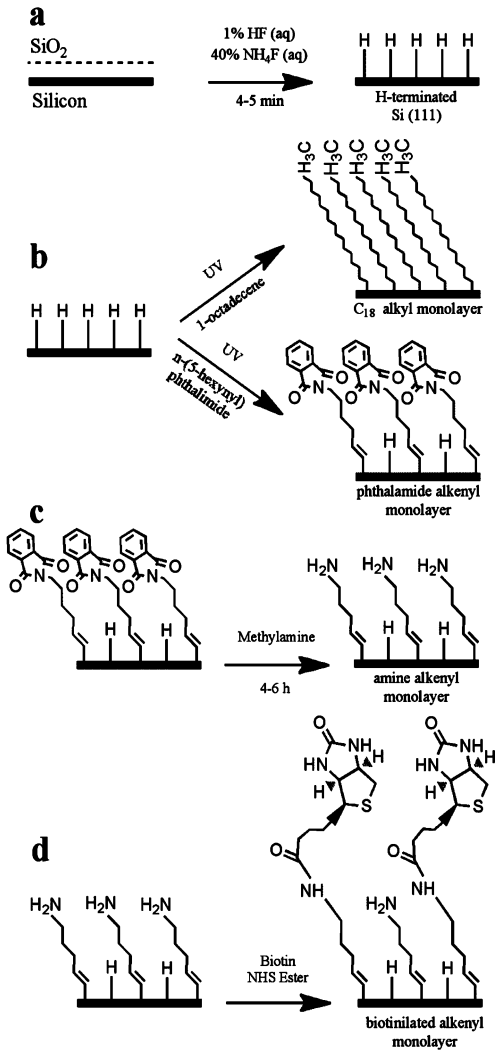

(a) Si—H surface formation: remove native SiO_2 with 1% HF (aq) followed by surface preparation with 40% NH_4F (aq). (b) Hydrosilylation UV reaction forming C_{18} alkyl and phthalimide alkenyl monolayers. (c) Deprotection of amine terminal groups. (d) Conjugate biotin to amine groups.

removal of the phthalimide groups (deprotection) with a methylamine solution, an amine terminal group (NH_2) was released for further conjugation.

The quality of the as-prepared monolayers was verified by using sessile drop contact angle measurements (see the Supporting Information, Table S1), and XPS on planar samples. A measured contact angle of 109° for the C_{18} alkyl monolayer indicates a high quality ordered monolayer on our planar and Si-NW surfaces. The XPS spectra were taken just after monolayer formation or after storage in dry nitrogen. Figure 4 shows representative XPS data for experimental samples. An etched piece of silicon was used as a reference. Figure 4a shows that the oxidation (103 eV) of the silicon surface exposed to UV irradiation for monolayer formation (red) is drastically reduced compared to the H—Si reference and piranha treated samples (blue and black, respectively). A survey spectrum of a phthalimide alkenyl monolayer on Si (111) (Figure 4b) shows the expected elements (Si, C, N, and O) indicating a clean contamination free surface. The silicon reference shows a small amount of carbon deposited on the surface, however, not the N1s peak (at 400 eV) thus discriminating the phthalimide monolayer. Deprotection of the monolayer exposes the NH_2 functional groups for further conjugation (Figure 4c). Figure 4c shows XPS results of the C1s region before and after deprotection. The monolayer following deprotection shows that the overall area percentage of C—N peak (286.57 eV) increases compared to the area of C—C (284.77 eV) as the carbon number decreased from 14 to 6 (Figures 4d, before and 4e, after deprotection). The peak at 288.55 eV (C═O) is expected to disappear after deprotection, but shows a decrease in percent area due to partial deprotection or some physically adsorbed C═O moieties on the surface (Figure 4e). Figure 4f shows XPS results from the N1s region of the spectrum following deprotection showing amine groups NH_2 and in the ammonium form NH_3^+ from the monolayer. High-resolution scanning electron microscopy was used to image the selective conjugation of thiolated Au nanoparticles coupled to the biotinylated Si-NW surfaces.

As previously described, this step requires the removal of the phthalimide protection groups to provide access to the NH_2 functional groups. Activated biotin was then conjugated to the NH_2-terminated surfaces. Gold nanoparticles conjugated with thiolated-streptavidin were then coupled to the biotinylated surfaces. Figure 5a shows an HRSEM image of a nonconjugated Si-NW. Figure 5b shows the selective conjugation of the Au nanoparticles to biotinylated all-(111) Si-NWs, and Figure 5c a zoomed image of the Si-NW surface.

Electrical characteristics have been measured using two different device configurations: capacitance—voltage (*CV*) characteristics of monolayer passivated electrolyte-insulator-silicon (EIS) structure with (111) surface planar silicon samples (Figure 6a) and current/front-gate voltage (*IV*) characteristics of Si-NWs with oxide and alkenyl monolayer dielectric layers (Figure 6b). The high frequency *CV* measurements demonstrate that the monolayer surfaces are uniformly passivated with an estimated monolayer thickness $t_m \approx 3$ nm (32), where $\varepsilon_m \approx 2$ is the relative permittivity of the monolayer (33) and A_c is the capacitor area. The most striking device performance improvement of monolayer passivated Si-NWs, compared to oxide passivated surfaces, is that the monolayer interfaces have improved electrical performance (Figure 6b), where device conductance can be modulated with very small front-gate voltages for $N_a \approx 1 \times 10^{17}$ cm^{-3}, which is not possible with the oxidized Si-NWs without back-gating (7).

The monolayers do not completely eliminate the interface effects as the measured device current with $V_{fg} = 0$ is $i_{ds} \approx$ 2 nA, which is lower than the ideal current $i_{ds} \approx$6 nA (34). The alkenyl monolayer passivated devices also show improved transconductance of $g \approx 63$ pA mV^{-1} compared to 36 pA mV^{-1} for a 10 nm oxide passivated Si-NW surface. The detection sensitivity is $\Delta G/G_o \approx 0.32$ for the alkenyl monolayer passivated Si-NWs with $h = 100$ nm compared to 0.04 for the oxidized Si-NW, an ~10× increase (35).

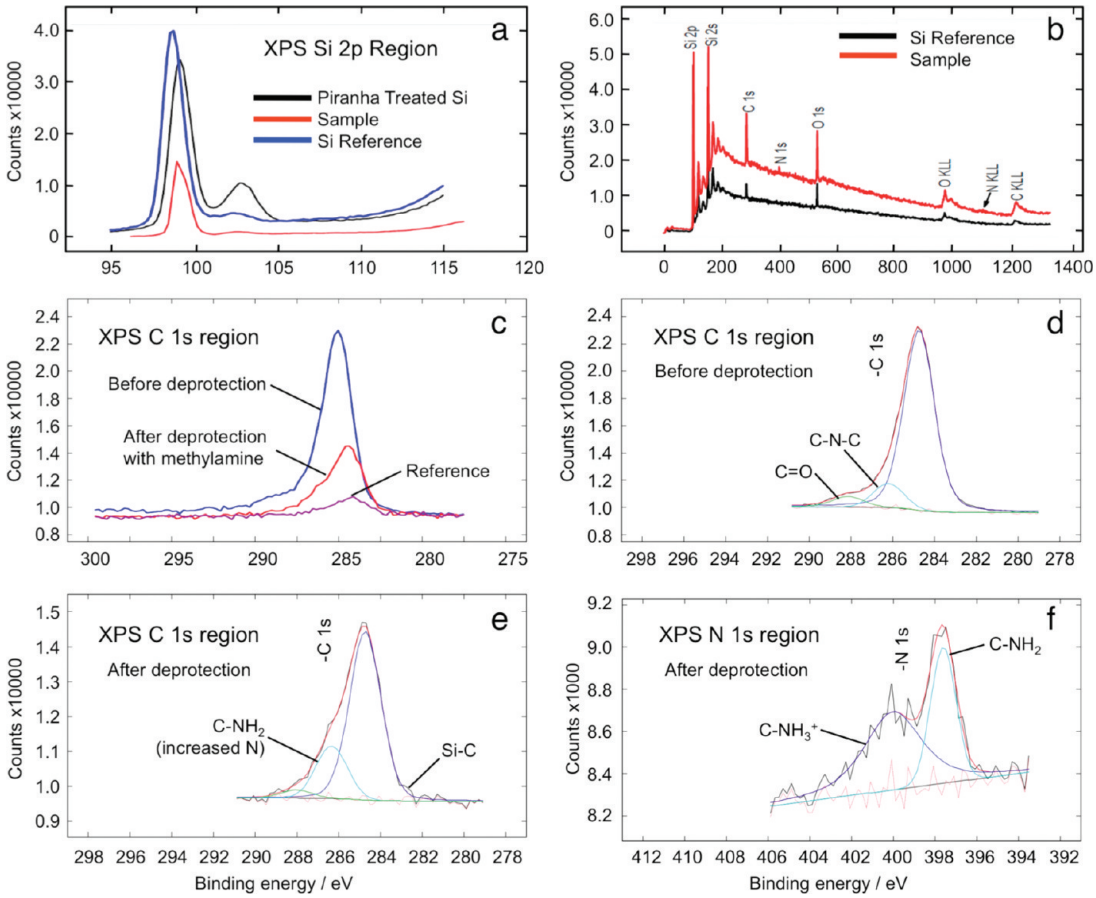

FIGURE 4. XPS results. (a) Si2p region (peak at 103 eV) shows oxidation of the silicon surface. (b) Survey spectrum of phthalimide monolayer on Si (111) surface (red) and silicon reference sample (black). (c) C1s region of the spectrum showing a comparison before and after deprotection. (d, e) C1s region shows fit for different functional bonds in the monolayer before and after deprotection. (f) N1s region after deprotection.

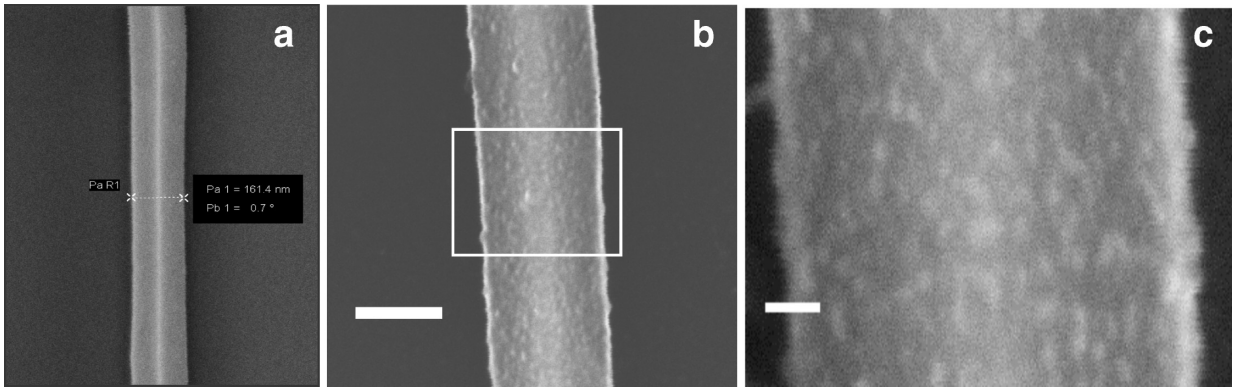

FIGURE 5. HRSEM images: (a) blank Si-NWs, (b) Si-NW surfaces following the conjugation of 5 nm diameter Au nanoparticles (scale bar 100 nm), (c) zoomed image of Si-NW surface (scale bar 20 nm).

In summary, the selective functionalization of C—Si monolayers on all-(111) surface Si-NWs has been demonstrated, which offers a new Si-NW sensing platform with several advantages for biosensing compared to conventional Si-NW biosensor geometries and silicon dioxide (SiO_2) passivation layers, which includes: (1) ligand conjugation exclusively on the nanowire surface, eliminating ligand conjugation in nonsensor region; (2) improved detection sensitivity; (3) Si-(111) surfaces supporting the highest-quality C—Si monolayers; (4) elimination of fixed SiO_2 charge; and (5) Si (111) surfaces can have low interface trap densities for H—Si and C—Si interfaces.

EXPERIMENTAL SECTION

Surface Preparation and Monolayer Formation. The samples were first cleaned to remove organic and metal impurities. The p-type planar Si (111) samples were cleaned with acetone and sonicated (10—20 min) and etched in 1% HF (1—2 min) to remove the native oxide. Etched silicon samples were rinsed with deionized H_2O and further cleaned with piranha solution (H_2O_2 30%, H_2SO_4 in 1:1 ratio) at 90 °C for 10 min and rinsed thoroughly with deionized H_2O. This procedure was repeated three times. The contact angle of the resultant surface was found to be zero (see the Supporting Information, Table S1). The p-type Si-NW samples were first cleaned with methanol, isopropanol, acetone and acetonitrile with low power sonication (5—20 min). The Si-NW samples were further cleaned with

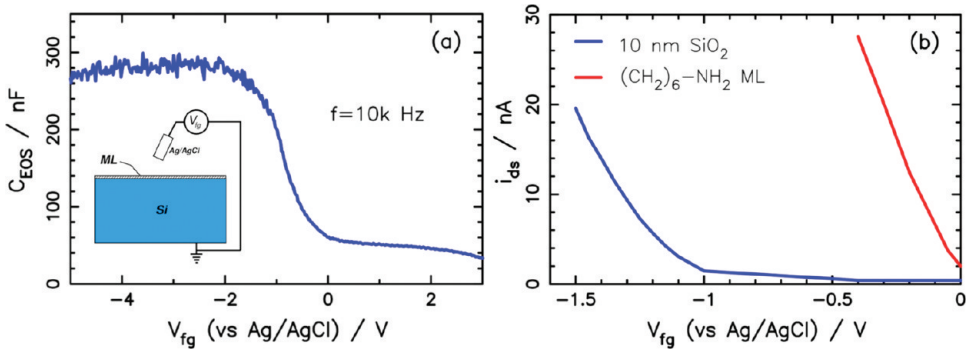

FIGURE 6. Electrical measurements: (a) high-frequency *CV* behavior of EIS structure with C_{18} monolayer passivation, (b) *IV* characteristics of Si-NWs with oxide (blue) and alkenyl monolayer (red) dielectric layers.

oxygen plasma (100W, 10 min). Silicon nanowire and planar samples were etched with 1% HF and NH_4F for 4−5 min and then rinsed thoroughly with deionized H_2O and placed into a custom-made vacuum vessel and the surface dried with a combination of vacuum (∼1 mTorr) and heating with an infrared lamp (Scheme 1a). The vacuum vessel (see the Supporting Information, Figure S2) was continuously purged with argon during the drying step. A thin layer of precursor solution was deposited onto the samples and irradiated for 4 h with a UV lamp (4.4 mW/cm^2 at 254 nm, Jelight Co., USA). The 40% NH_4F etchant and 0.2 M precursor solution in mesitylene were bubbled with pure argon gas for 1 h before the hydrosilylation reaction. After the hydrosilylation reaction, the samples were exposed to ambient air and sonicated with dichloromethane, chloroform, methanol, and acetonitrile.

AFM Imaging. A Digital Instruments Dimension 3100 was used for all AFM images. All AFM images performed in tapping mode with ultra sharp (average tip diameter ∼2 nm) single-crystal silicon tips (SSH-NCH-10, NanoandMore, Gmbh).

XPS Characterization. XPS characterization has been conducted with a monochromatic X-ray beam (Al Kα, 1486.6 eV, 100W, Quantera, Physical Electronics). Mapping was done at 3×10^{-9} Torr and detector angles of 70 and 45°. XPS spectra were taken just after monolayer formation or after storage in a dry nitrogen box.

HRSEM Imaging. For deprotection of the phthalimide groups, samples were placed in a 30% methylamine solution in ethanol for 6−8 h (Scheme 1c). Following the reaction, the samples were rinsed with triethylamine and ethanol, and subsequently nitrogen dried. Activated biotin (Sigma Aldrich) was conjugated to the amine-terminated surfaces by placing the samples in a 3 mM solution of activated biotin/DMF for two hours at room temperature. After the reaction they were sonicated in DMF, ethanol, and acetone (5−10 min.). Gold nanoparticles conjugated with streptavidin (0.25 mL streptavidin conjugated Au nanoparticles in solution (5 nm average diameter, Ted Pella, Inc. USA) was diluted to 100 mL of solution by adding 20 mM Tris buffer, 154 mM NaCl, and deionized H_2O. The biotinylated surfaces were immersed with the labeling solution for 12 h at room temperature. Monolayers prepared by 1-octadecene do not include a deprotection step and biotinylation.

Numerical Simulations. 2D finite element simulations were performed using commercial simulation packages Tsuprem-4 Version C-2009.06 and Medici Version A-2007.12, Synopsys, Inc.

Electrical Measurements. Si-NW devices were first encapsulated with a polyimide layer (thickness: 2 μm), followed by wire-bonding to a custom printed circuit board and finally all electrical wires and contacts were sealed with an epoxy (Hysol, Henkel Corporation). Following encapsulation, the Si-NW oxide surfaces were cleaned with UV ozone (UV/Ozone Pro Cleaner, Bioforce, Inc.). The monolayers were formed as previously described following the removal of the gate oxide. Electrochemical measurements were done in a 10 mM universal buffer mixture (UBM) (0.1 M citric acid, 0.1 M sodium dihydrogen phosphate, 0.2 M boric acid, and 0.1 M NaCl) at pH 2.8. The CV measurements were recorded with an impedance analyzer (Hewlett-Packard 4194A Impedance Gain-Phase Analyzer) at a frequency of 10 kHz and the front-gate voltage, using a reference electrode (REF200 Ag/AgCl, Radiometer Analytical) was swept from -5 V $\leq V_{fg} \leq +2$ V. The *IV* characteristics of the Si-NWs was measured with a lock-in amplifier (SR830, Stanford Research Systems) with $v_{ds} = 50$ mV, 30 Hz modulation frequency, and $V_{bg} = 0$. A reference electrode (REF^{200} Ag/AgCl, Radiometer Analytical) in 10 mM UBM at pH 2.8 buffer solution and the applied the front-gate voltage and was swept from -1.5 V$\leq V_{fg} \leq 0$ V for oxide passivated devices and swept from -0.4 V$\leq V_{fg} \leq 0$ V for the alkenyl monolayer passivated Si-NW devices.

Acknowledgment. Thanks to Johan Bomer, Jan van Nieuwkasteele, and Hans de Boer for technical assistance with silicon nanowire fabrication and construction of the reaction vessel, and thanks to Gerard Kip for XPS measurements and Mark Smithers for high-resolution scanning electron microscopy imaging. The project was funded by the Higher Education Commission (HEC)/Government of Pakistan.

Supporting Information Available: Results of surface charge transconductance calculations (PDF). This material is available free of charge via the Internet at http://pubs.acs.org/.

REFERENCES AND NOTES

(1) Cui, Y.; Wei, Q. Q.; Park, H. K.; Lieber, C. M. *Science* **2001**, *293*, 1289.
(2) Bunimovich, Y. L.; Shin, Y. S.; Yeo, W.; Amori, M.; Kwong, G.; Heath, J. R. *J. Am. Chem. Soc.* **2006**, *128*, 16323.
(3) Gao, Z. Q.; Agarwal, A.; Trigg, A. D.; Singh, N.; Fang, C.; Tung, C. H.; Fan, Y.; Buddharaju, K. D.; Kong, J. M. *Anal. Chem.* **2007**, *79*, 3291.
(4) Patolsky, F.; Lieber, C. M. *Mater. Today* **2005**.
(5) Wanekaya, A. K.; Chen, W.; Myung, N. V.; Mulchandani, A. *Electroanalysis* **2006**, *18*, 533.
(6) Tong, H. D.; Chen, S.; van der Wiel, W. G.; Carlen, E. T.; van den Berg, A. *Nano Lett.* **2009**, *9*, 1015–1022.
(7) Chen, S.; Bomer, J. G.; van der Wiel, W. G.; Carlen, E. T.; van den Berg, A. *ACS Nano* **2009**, *3*, 3485.
(8) Buriak, J. M. *Chem. Rev.* **2002**, *102*, 1272.
(9) A ligand refers to a receptor biomolecule attached to the sensor surface. An analyte refers to the complementary biomolecule in the solution. A ligand-analyte pair is a selectively hybridized biomolecular conjugate.
(10) van der Voort, D.; McNeil, C. A.; Renneberg, R.; Korf, J.; Hermens, W. T.; Glatz, J. F. C. *Sens. Actuator, B* **2005**, *105*, 50.
(11) Bunimovich, Y. L.; Ge, G.; Beverly, K. C.; Ries, R. S.; Hood, L.; Heath, J. R. *Langmuir* **2004**, *20*, 10630.

(12) Park, I.; Li, Z.; Pisano, A. P.; Williams, R. S. *Nano Lett.* **2007**, *7*, 3106.
(13) Zhang, G.-J.; Zhang, G.; Chua, J. H.; Chee, R. E.; Wong, E. H.; Agarwal, A.; Buddharaju, K. D.; Singh, N.; Gao, Z.; Balasubramanian, N. *Nano Lett.* **2008**, *8*, 1066.
(14) Doping concentration dependent carrier mobility has been included in all calculations.
(15) Sze, S. M. *Physics of Semiconductor Devices*, 2nd ed.; John Wiley & Sons: New York, 1981.
(16) The calculated sensitivity data is normalized to the maximum sensitivity occurring for $t_f = 1$ nm and $N_a = 1017$ cm^{-3} at $\Psi_o = 0$. For the surface charge sensitivity calculation, $\varepsilon_w = 80$ and $c_o = 10$ mM.
(17) Israelachvili, J. *Intermolecular and Surface Forces*, 2nd ed.; Academic Press: London, 1992.
(18) Fritz, J.; Cooper, E. B.; Gaudet, S.; Sorger, P. K.; Manalis, S. R. *Proc. Natl. Acad. Sci. U.S.A.* **2002**, *99*, 14142.
(19) Kar, S.; Miramond, C.; Vuillaume, D. *Appl. Phys. Lett.* **2001**, *78*, 1288.
(20) Weldon, M. K.; Queeney, K. T.; Eng Jr., J.; Raghavachari, K.; Chabal, Y. J. *Surf. Sci.* **2002**, *500*, 859.
(21) Leão, C. R.; Fazzio, A.; da Silva, A. J. R. *Nano Lett.* **2007**, *7*, 1172.
(22) Scheres, L.; Giesbers, M.; Zuilhof, H. *Langmuir* **2010**, *26*, 4790.
(23) Wu, Y.; Cui, Y.; Huynh, L.; Barrelet, C. J.; Bell, D. C.; Lieber, C. M. *Nano Lett.* **2004**, *4*, 433.
(24) Choi, Y.-K.; Lee, J. S.; Zhu, J.; Somorjai, G. A.; Lee, L. P.; Bokor, J. *J. Vac. Sci. Technol., B* **2003**, *21*, 2951.
(25) Stern, E.; Klemic, J. F.; Routenberg, D. A.; Wyrembak, P. N.; Turner-Evans, D. B.; Hamilton, A. D.; LaVan, D. A.; Fahmy, T. M.; Reed, M. A. *Nature* **2007**, *445*, 519.
(26) Yablonovitch, E.; Allara, D. L.; Chang, C. C.; Gmitter, T.; Bright, T. B. *Phys. Rev. Lett.* **1986**, *57*, 249.
(27) Cheng, Y. C. *Prog. Surf. Sci.* **1977**, *8*, 181.
(28) Bent, S. F. *Surf. Sci.* **2002**, *500*, 879.
(29) Puniredd, S. R.; Assad, O.; Haick, H. *J. Am. Chem. Soc.* **2008**, *130*, 13727.
(30) Zuilhof, H.; Sudholter, E. J. R. *Adv. Mater.* **2000**, *12*, 1457.
(31) Ciero, R. L.; Chidsey, C. E. D. *Langmuir* **2002**, *18*, 305.
(32) The monolayer thickness has been estimated with $t_m \approx \varepsilon_m \varepsilon_o A_c / C_{EOS}$, with $A_c = 0.5$ cm^2.
(33) Gorostiza, P.; de Villeneuve, C. H.; Sun, Q. Y.; Sanz, F.; Wallart, X.; Roukherroub, R.; Allongue, P. *J. Phys. Chem. B* **2006**, *110*, 5576.
(34) The maximum ideal current in the undepleted triangular is $i_{ds} \approx q\mu_b N_a v_{ds} L^{-1} wh/2$ with $\mu_b \approx 300$ cm^2 V^{-1}s^{-1}, $N_a = 1 \times 10^{17}$ cm^{-3}, $v_{ds} = 100$ mV, $L = 10\ \mu$m, $h = 100$ nm, and $w = 2h/\tan(54.74°)$, where μ_b is the concentration-dependent hole mobility.
(35) The alkenyl monolayer Si-NW sensitivity was estimated for $\Delta\psi = 10$ mV: $G_o = 2$ nA/v_{ds} and $G = 63$ pA/mV $\times$ 10 mV/$v_{ds} = 0.63$ nA/v_{ds} and $\Delta G/G_o = 0.315$. The oxide Si-NW sensitivity was estimated for $\Delta\psi = 10$ mV: $G_o = 10$ nA/v_{ds} and $G = 36$ pA/mV $\times$ 10 mV/v_{ds} =0.36 nA/v_{ds} and $\Delta G/G_o = 0.036$.

AM100922E